ADVANCED ENGINEERING MATERIALS
www.aem-journal.com

3D Graphene Foam Reinforced Low-Temperature Ceramic with Multifunctional Mechanical, Electrical, and Thermal Properties

*Tony Thomas, Cheng Zhang, Pranjal Nautiyal, Benjamin Boesl, and Arvind Agarwal**

Graphene foam reinforced multifunctional ceramic composite is fabricated in this study. Graphene foam has a 3D macroporous architecture, which is filled with a low temperature co-fired (LTCC) ceramic phase. The composite microstructure is engineered by three-step fabrication scheme: infiltration of porous graphene foam with ceramic slurry, solidification to form a green body, and finally, pressure and temperature-assisted sintering to produce a dense composite with intimate ceramic/graphene interface. Graphene foam is found to retain its 3D structure. The interconnected network of nodes and branches induces superior fracture toughness, load-bearing capacity, and thermal – electrical transport characteristics. Addition of mere 0.18 wt% graphene foam results in a 480% improvement in the fracture energy. Subsurface examination reveals extensive crack deflection due to graphene foam's cellular units, highlighting the advantage of a 3D filler. Graphene foam also induces an impressive electrical conductivity of 165 S m^{-1} in an otherwise insulator ceramic. In situ infrared thermal imaging demonstrates enhanced thermal transportability in ceramic due to graphene foam. These findings attest the significance of 3D graphene foam to develop multifunctional ceramic composites in load-bearing structures, thermal management, and electro-mechanical devices. The synthesis scheme presented here is promising for facile and scalable manufacturing of this new class of materials.

1. Introduction

2D graphene has been at the center stage of attention for developing new composite materials with unprecedented properties and advanced applications.[1–8] Owing to its extraordinary mechanical, thermal, and electrical properties,[9–11] graphene addition has found to improve strength, toughness, stiffness, and thermal-electrical conductivity of ceramic materials.[1–12] Despite the fanfare around graphene's excellent *intrinsic* properties, there are numerous practical challenges associated with engineering the ceramic composites with desired microstructure and predictable properties. Graphene flakes tend to agglomerate and form clusters due to intermolecular $\pi-\pi$ interactions.[13] These agglomerates act as stress concentrators in the microstructure and lead to failure initiation upon mechanical loading.[14] Lack of homogeneous distribution also impedes electron and phonon conduction, limiting the electrical and thermal properties of the composites. To overcome these challenges, various physical and chemical dispersion techniques are adapted to effectively integrate graphene into the ceramic matrix. Some of the examples are ball milling, sonication, centrifugation, surface modification, functionalization, and a combination of these approaches.[15–22] However, there are various disadvantages associated with these techniques: they are time-consuming, expensive, involve the addition of chemicals/secondary particles which lead to undesirable impurities and can cause physical and chemical damage of the graphene flakes. Additionally, due to their 2D morphology, the varying degrees of alignment of graphene flakes in the matrix can lead to highly anisotropic and inconsistent properties. These challenges related to processing and microstructure control in graphene-ceramic composites are major bottlenecks in bulk scale manufacturing and real-world application of this promising class of nanocomposites.

One potential approach to simplify the processing and improve the microstructure homogeneity is to use free-standing 3D architectures of graphene as the filler material in the composite.[23–29] Macroporous graphene foam (GrF) has emerged as a promising filler material for developing composites.[30–37] GrF consists of an interconnected network of nodes and branches, providing seamless pathways for transfer of stresses, electrons, and phonons. As a result, this material displays remarkable flexibility and resistance to failure,[38,39] damping capability,[40,41] and brilliant electrical and thermal conductivities.[42,43] GrF has an ultra-low density (<5 mgcm^{-3}), high surface area (≈850 m^2g^{-1}) and pore size exceeding 500 µm. This hierarchical structure of GrF has been exploited to infiltrate it with polymer resin followed by curing, creating a composite material with a defined and homogeneous distribution of filler

T. Thomas, C. Zhang, P. Nautiyal, B. Boesl, Prof. A. Agarwal
Plasma Forming Laboratory
Department of Mechanical and Materials Engineering
Florida International University
10555 West Flagler Street, EC 3474, Miami 33174, USA
E-mail: agarwala@fiu.edu

The ORCID identification number(s) for the author(s) of this article can be found under https://doi.org/10.1002/adem.201900085.

DOI: 10.1002/adem.201900085

phase.[30,35–37,41–43] The introduction of a pre-fabricated 3D foam does not require complex dispersion techniques, provides superior microstructure control and uniform properties. GrF-reinforced composites have shown to be desirable for application in strain sensors,[32,43] supercapacitor,[25] electrochemical biosensors,[44] biocompatible scaffolds,[29] electromagnetic shielding,[33] fuel cells,[45] thermal interfacing,[38] acoustic backing,[46] vibration damping,[40,41] and as structural materials with enhanced resistance to failure.[35,42] Most of the GrF-based composites and their applications reported in the literature are polymer-based due to ease of processing.[37] Recently, graphene foam's desirable mechanical attributes were also exploited to develop a metallic metamaterial with ultra-high stiffness, damage tolerance, and fatigue resistance.[38]

There are reports on GrF-ceramic composites for applications in Li-ion batteries,[47] supercapacitors,[48] biosensors,[49] and high-performance electromagnetic interference shielding.[50] These applications require high surface area, and hence the developed composites are porous with a deposition or decoration of ceramic on GrF surface. Application of 3D GrF to develop a dense, non-porous ceramic matrix composite for structural applications is unexplored. We envisage that 3D graphene foam's interconnected network of branches can be exploited to render unprecedented toughness and stiffness in a dense ceramic by facilitating extensive stress transfer, crack deflection, and crack absorption. The toughening and stiffening mechanisms reported for 2D graphene-based composites are rather localized due to the discrete nature of the reinforcement phase.[13] This makes 3D contiguous GrF a potential and promising filler for ceramic matrix composites. Addition of GrF will also aid in the simultaneous enhancement of electrical and thermal properties, inducing multi-functionality in the composite materials. However, the processing and densification of ceramics require the application of relatively higher temperatures and pressures. A major challenge is to preserve the structural integrity of GrF during ceramic densification.

We propose a novel three-step route for engineering dense 3D GrF-ceramic composites: i) infiltration of ceramic slurry in GrF; ii) drying/solidification of the slurry; and iii) pressure-assisted sintering of the ceramic-filled GrF. The first two steps provide a structural backbone to an otherwise porous GrF, as it is filled and surrounded by a solidified ceramic phase. This ceramic-GrF green body can subsequently be sintered without compromising the 3D interconnected architecture of GrF. Here, a low temperature co-fired ceramic (LTCC) composed of Alumina and Silica phases is chosen as the ceramic matrix. Spark plasma sintering technique is used for rapid densification and achieving intimate ceramic/graphene interfacial contact in the composite. LTCC have widespread applications in packaging of electronic systems in automotive, military, space, medical, and industrial installations.[51] One of the most common application of LTCC is in the integration of Microelectromechanical systems (MEMS). Superior mechanical properties and thermal transport are desirable in LTCC for structural stability, thermal management, and product reliability. 3D GrF can be promising filler material for simultaneous enhancement of mechanical and thermal properties of LTCC. In this study, the effect of GrF filler on the load bearing ability of LTCC is examined by *high load* instrumented indentation testing. The associated toughening and strengthening mechanisms are closely examined by surface and sub-surface electron microscopy. The thermal transport is probed by in situ infrared thermal imaging at elevated temperatures. The effect of GrF addition on electrical transport is evaluated by measuring the electrical conductivity of the composite. The approach presented here can be employed for engineering a new class of multifunctional ceramic composite materials with microstructural homogeneity, and superior mechanical and transport properties.

2. Results and Discussions

2.1. Fabrication Methodology Development

The real challenge in fabricating a dense ceramic with fully embedded GrF is the preservation of highly reticulated 3D foam structure under high pressure and temperature conditions required to consolidate ceramic. Hence, GrF reinforcement is mostly limited to low viscous polymers[36,42,52] or in the fabrication of macroporous material with GrF as the scaffold.[53] Freestanding GrF, by itself, should be delicately handled. Subjecting it to high pressure would collapse the cell structure and would void the absolute purpose of retaining interconnected and continuous structure. The paramount objective of the developed fabrication technique is to produce dense GrF/ceramic material while still preserving GrF's reticulated cell structure. Hence a three-step fabrication technique was developed as represented by the schematic in **Figure 1**. The first step is the infiltration of $10 \times 10\,mm^2$ GrF by a low viscous LTCC slurry as shown in Step 1 of the schematic in Figure 1. The LTCC ceramic slurry had 32 wt% of solid loading along with 0.57 wt% of fish oil dispersant dispersed in terpineol solvent. **Figure 2**a gives a perspective of the pore size and shape of the free-standing GrF used in this study. Figure 2b is the powder morphology of the LTCC. The average particle size is $<3\,\mu m$ and can be packed within the pores of the GrF which is approximately $540\,\mu m$. The irregular shape of the LTCC powder particle will further assist in efficient powder packing during SPS. The slurry composition was formulated according to the infiltration factor (I_f).[42] It constitutes of the ratio of the cell size of the GrF to the viscosity of the infiltrate. For efficient infiltration, Embery et al.[42] reported that the I_f should be greater than $1\,\mu m\,cP^{-1}$. Terpineol has a viscosity of 36.5 cP at RT.[54] The LTCC slurry, after 1 h of ball milling recorded a viscosity of 80 cP at RT. For a given GrF cell size of $540\,\mu m$, the I_f was $6.75\,\mu m\,cP^{-1}$. As per infiltration factor postulation ($I_f > 1\,\mu m\,cP^{-1}$), the slurry infiltrated the GrF efficiently, converting the open cell GrF to completely closed cell GrF as shown in Step 1 of the schematic in Figure 1. Step 2 mainly constitutes of evaporating the solvent and solidifying the infiltrated LTCC slurry. This was achieved by a two-step heat treatment process. Initially, the infiltrated GrF was heated to 75 °C for 30 min to evaporate the solvent and consecutively heated to 850 °C for 20 min in an argon atmosphere for complete solidification. Now this solidified encapsulant in the pores of the GrF acts as a protective barrier by imparting load-bearing functionality. As a result, any external pressure would still maintain the GrF's reticulated structure due to confinement of GrF cells by the infiltrated LTCC. If this novel

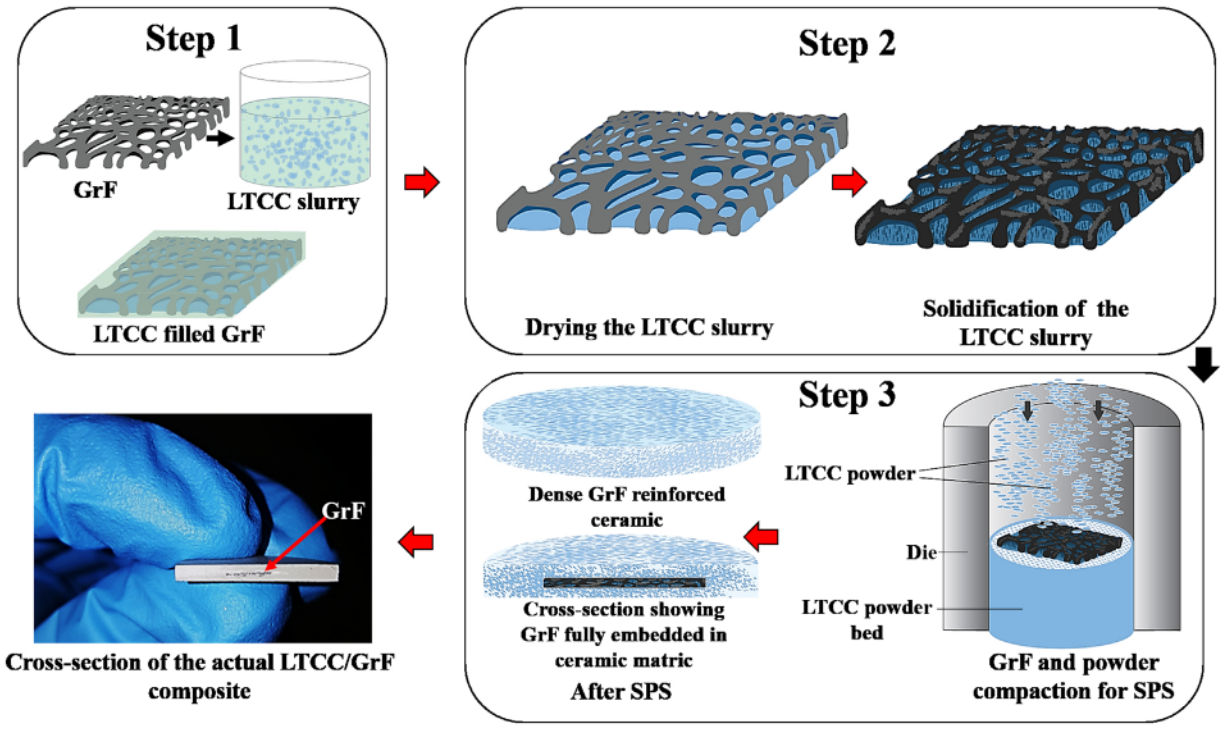

Figure 1. Schematic of the three-steps fabrication methodology developed to produce full embedded closed cell GrF reinforced ceramic.

process were to be adopted in the fabrication of electronic packaging for medical implants, the electronic circuit is designed, and circuit components are embedded on the GrF in Step 1 of the process. The solidified LTCC around the electronic circuitry will protect the circuit elements from external pressure thus increasing the robustness of the implants. Steps 1 and 2 are the crucial steps in this novel ceramic/GrF processing technique.

The preservation of reticulated GrF foam structure was meticulously monitored during all the stages of fabrication. **Figure 3** is the SEM image showing the top surface of the LTCC/GrF after Step two of the fabrication process. Features like nodes and branches are intact as seen in Figure 3. It should be noted that the Step 1 infiltration process was pressureless resulting in gravity assisted infill by LTCC slurry. The surface seen in Figure 3 looks relatively dense with a good bonding between the graphene and LTCC. The bonding is purely mechanical as the processing condition for the LTCC (primarily oxides) and carbon to react and form a different phase was limited. The debonded region shown in the inset in Figure 3 is the hollow strut of the GrF resulted from etching of the Ni scaffold[40] during the GrF fabrication process through CVD. The hollow struts are about 30–50 μm in

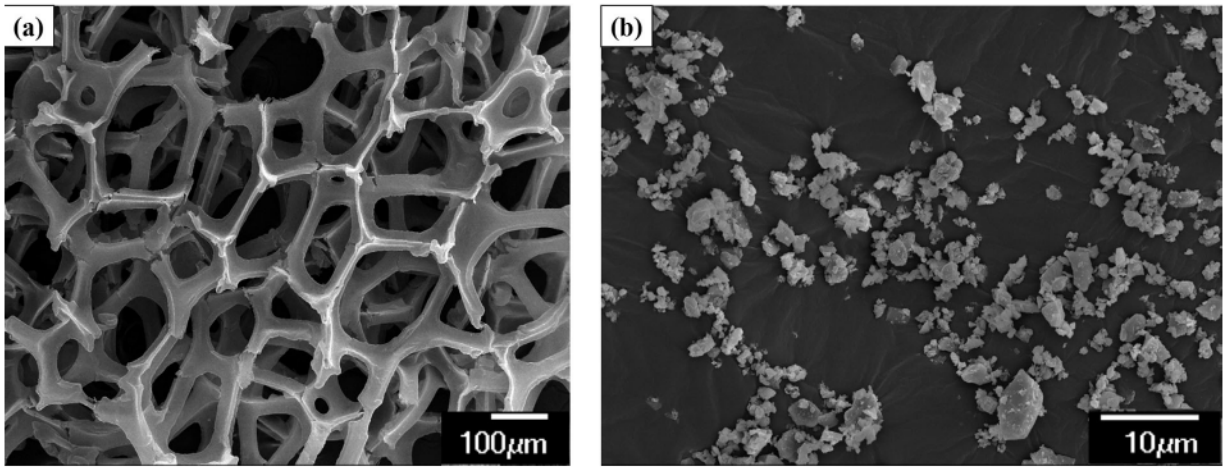

Figure 2. a) SEM image of freestanding GrF; b) powder morphology of LTCC.

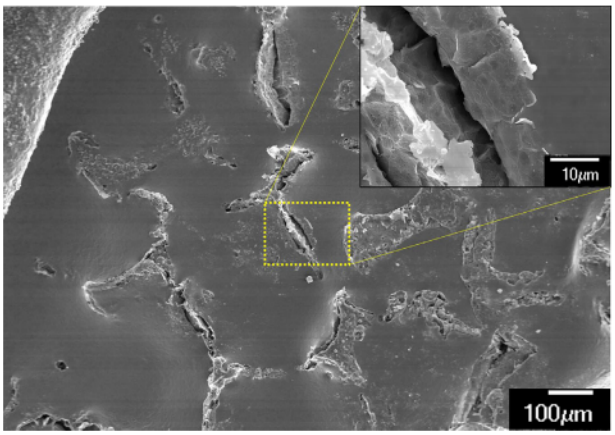

Figure 3. SEM image is showing the survival of GrF after step two of the fabrication process. Inset is the SEM image of hollow GrF strut.

diameter. Though the average particle size of LTCC powder is <3 μm, the infiltration failed to fill these hollow struts. Embert et al.[42] suggested that in the case of resin type infiltration, the hollow struts are filled due to the capillary action driven by Laplace pressure. Unfortunately, the Laplace pressure can only act on liquid, and it has a less profound effect on the micron-sized solid particles as in this case. The inset is shown in Figure 3 also assures intimate bonding of GrF's branches with the sintered LTCC. These hollow interfacial profile can be eliminated by consolidation via SPS.

The final Step 3 as seen in the schematic (Figure 1), is the densification of LTCC/GrF packaging by Spark Plasma Sintering (SPS). The infiltrated GrF is sandwiched between LTCC powder beds in a graphite die. The die is subjected to the sintering conditions stated in the experimental section to obtain a dense ceramic reinforced with GrF with its reticulated structure intact. The bottom left image in the schematic (Figure 1) shows a photograph of the LTCC/GrF composite after SPS. From the optical images shown in **Figure 4**a and b, it is evident that even after the GrF is subjected to high temperature and pressure during SPS, the reticulated structure of the GrF is intact. The presence of silica in the LTCC composition enabled effective densification of the ceramic at an SPS temperature as low as 700 °C. Moreover the GrF in the ceramic amplified the thermal and electrical conductivity in the material system,[38,39] resulting in high-density ceramic/foam composite at a low temperature of 700 °C as seen in Figure 4. The sintered LTCC/GrF composite was 97.2% dense (true density), whereas the pure LTCC was 98.5% dense (true density). The reduction of 1.3% density in LTCC/GrF composite is due to the presence of hollow struts of the GrF as shown in Figure 3 inset.

The infiltrated LTCC slurry delivered adequate support for the GrF to withstand the 100 MPa pressure applied during SPS. The hexagonal profile of the embedded GrF (refer Figure 4a), along with its branches and nodes (refer Figure 4b) are visible in the SPS consolidated LTCC. Moreover, the hollow branches as shown in the inset in Figure 3, collapsed into layers of graphene after sintering. A recent study showed that the diamond-like configuration of two-layered graphene exhibit outstanding elastic modulus.[55] Hence the collapsed branches in addition to cells filled with LTCC are desirable for enhanced load bearing and stress transfer functionality in the material.

2.2. Fracture Energy of LTCC/GrF Composite

The effect of GrF reinforcement on the mechanical properties of LTCC was evaluated using *high load (100 N)* instrumented indentation technique. Indentation test was performed on the polished cross-section of pure LTCC and LTCC/GrF composite samples. **Figure 5** is the load- displacement graph portraying the behavior of the samples under uniaxial compressive load in the displacement control mode.

For a similar displacement of 0.25 mm, LTCC/GrF can withstand ≈4 times the load as pure LTCC (Figure 5). The displacement recovery of the LTCC/GrF material is ≈23% compared to pure LTCC. GrF is known for its super-elastic metamaterial properties.[23,38] This creates a site for efficient energy dissipation thus absorbing the deformation energy caused by loading. The area under the force-displacement curve in Figure 5 represents the energy absorbed by the material upon deformation and fracture. The fracture energy for LTCC/GrF composite is 7.54 mJ as compared to 1.3 mJ for pure LTCC. A mere 0.18 wt% GrF reinforcement induced ≈480% improvement in the fracture energy of the LTCC. Due to the intrinsic brittle nature of the LTCC, the energy dissipated during high load indentation is released in the form of cracks nucleated from the indent. The measured crack length was ≈1031.2 μm for pure LTCC as compared to a much shorter crack length (215.5 μm) for LTCC/GrF composite as shown in Figure S1, Supporting Information. To establish the dominant fracture mechanism in LTCC/GrF composite, the crack generated by indentation was investigated by Focused Ion Beam (FIB)-SEM as shown in **Figure 6**. Inset in Figure 6a, is a crack emanated from a region slightly below the indent. It is intriguing to notice the profile of this particular crack. It does not propagate as a continuous line, instead the crack manifest as a discontinuous "dashed line" like. Figure 6a is the FIB-SEM of the sub-surface showing the crack which deflected 90° out-of-plane. This suggests that GrF alters the behavior of crack propagation and crack deflection can be the underlying dominant fracture mechanism as multiple crack deflection can be witnessed in Figure 6b.

A 2D mechanical analysis of cellular GrF structure was conducted to establish tangible reasoning for crack deflection. For this purpose, the strain experienced by individual GrF cell upon loading in-plane was analyzed. As the majority of the cell is hexagonal (refer Figure 2a), the strain analysis was carried out on a hexagonal cell as shown in **Figure 7** schematic. During the point of the study, the strain exerted by the infiltrate is neglected. The strain (ε) in-plane for various loading was evaluated using Equation (1):[56]

$$\varepsilon = \frac{\delta \sin\theta}{l \cos\theta} \tag{1}$$

where cell wall deflection δ for the applied load P as shown in Equation (1) is represented by Equation (2):[56]

$$\delta = \frac{P l^3 \sin\theta}{12\, E\, I} \tag{2}$$

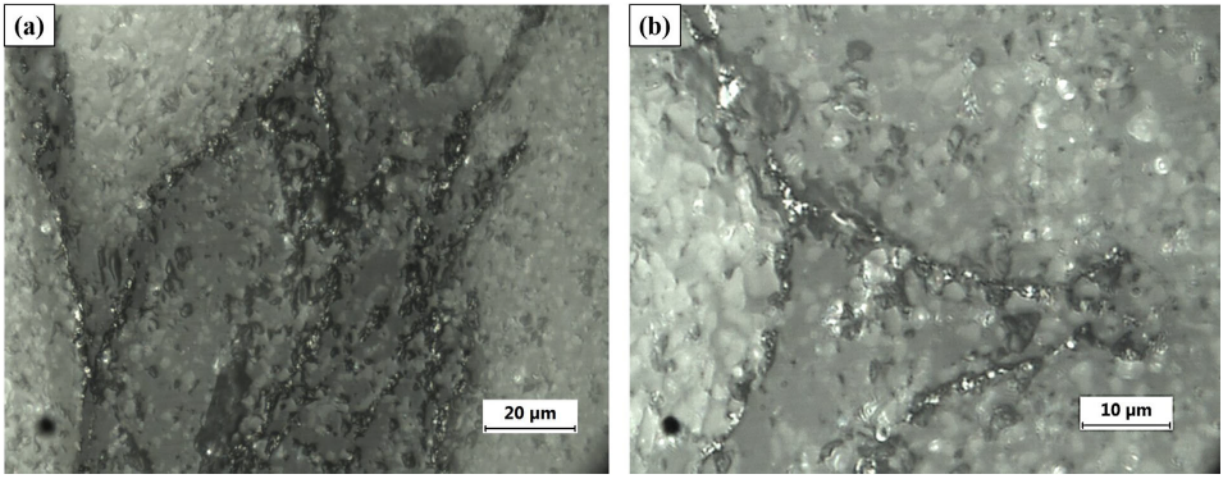

Figure 4. Optical images of the LTCC/GrF cross-section after SPS. a) Image showing hexagonal geometry of the GrF cell; b) Image showing untampered branches and nodes of the GrF foam embedded in the ceramic.

In Equations (1) and (2), l and θ are the cell geometry as shown in Figure 7a, P is the applied load, E is the elastic modulus of graphene, which is taken as 1 TPa[38] in this theoretical analysis and I is the moment of inertia of the wall cross-section (considered as a triangular cross-section). Based on Equations (1) and (2), it was theoretically calculated that for a maximum applied load of 100 N (the load applied during indentation test in this study), the GrF experience a negligible deflection (Figure 7b) and strain of 2.5×10^{-11} mm and 1.8×10^{-13}, respectively. This is mainly due to the high elastic modulus of the graphene. As a result, the propagating crack instead of penetrating through the GrF strut is deflected 90° out-of-plane as seen by FIB-SEM in Figure 6. For the crack to propagate through the graphene strut, the critical load required is given by Equation (3):[57]

$$P_{critical} = \frac{n^2 \pi^2 EI}{h^2} \tag{3}$$

where h is the length of the strut as represented in Figure 7a and n is a factor representing the rotational stiffness of the node. For a regular hexagonal honeycomb structure, if $h/l = 1$, $n = 0.686$ and for $h/l = 2$ the $n = 0.806$.[57] For $n = 0.686$, the $P_{critical}$ is 0.1 TN and for $n = 0.806$ the $P_{critical}$ is 0.14 TN. The theoretical $P_{critical}$ based on the cell geometry predicts a critical load of ≈0.1 TN is required for a crack to propagate through graphene strut. Also from Equation (3), it can be interpreted that a higher value of h/l ratio, increases rotational stiffness of the node (n) which in turn increases the fracture energy of the individual hexagonal cells. From the following individual strut analysis, it can be concluded that the GrF used in the fabrication of LTCC/GrF composite has a higher value of h/l ratio, thereby increasing the stiffness of the strut. The stiffer GrF struts prevented the propagation of the crack through the GrF and instead deflected the crack 90° out-of-plane, thus tremendously increasing the fracture toughness of the composite material. From the material design point of view, a material reinforced with higher h and a lower l GrF cell geometry can enhance the fracture energy in the so formed material. This set of analysis can be used in the design of GrF to induce tailored mechanical strength in materials being reinforced, but that is not the goal of the current study.

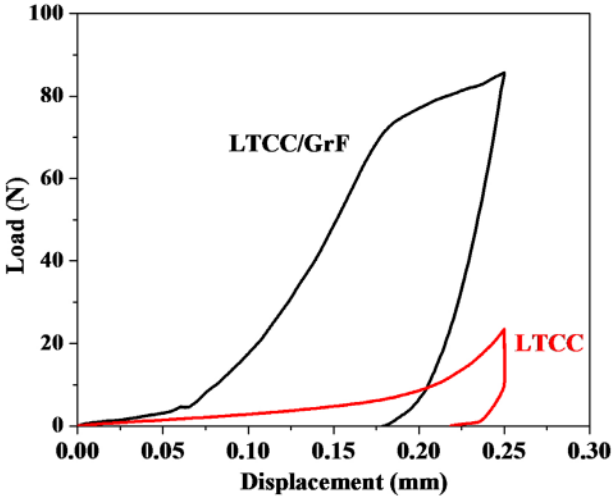

Figure 5. Force – displacement graph of LTCC and LTCC/GrF material obtained from high load indentation.

2.4. Electrical and Thermal Properties of GrF-LTCC Composite

To establish the influence of GrF on the electrical property of LTCC, a four-point probe DC electrical characterization at room temperature and the pressure was conducted. Pure LTCC (Dupont 951) is an electrically insulating material with a dielectric constant of 7.8. Hence they are widely used in the fabrication of micro-resistors and micro-capacitors. Due to the high electrical resistance above the range of DMM used, no specific resistance value was

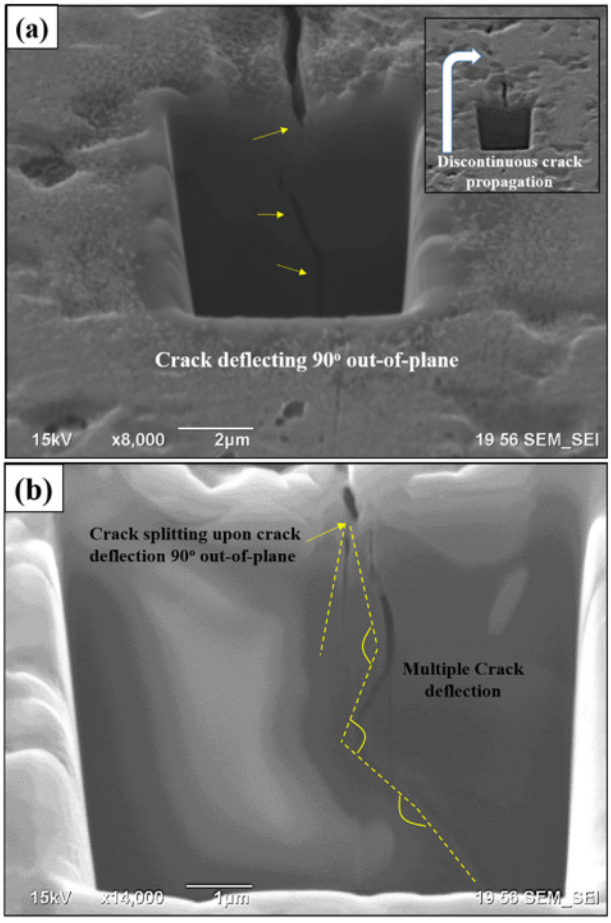

Figure 6. a) FIB-SEM revealing crack deflection 90° out-of-plane, (b) Multiple crack deflection of crack in LTCC/GrF material.

obtained for pure LTCC, and hence the conductivity is not reported here. As the GrF was embedded, the LTCC/GrF's electrical conductivity was dominated by the GrF intrinsic property, and the material recorded a total electrical conductivity of 165 S m^{-1}. The high electrical conductivity in 3D GrF which is $\approx 10^6$ S m^{-1}[30] stems from the adjacent graphene sheets bonded by van der Waals force presenting contact conductance as shown by the schematic in **Figure 8**. Schematic in Figure 8 shows two Gr sheets and the charge transfer between the sheets and across the sheets, thus increasing the electron transfer surface per unit area of the foam, making GrF highly electrically conductive. Liu et al.[58] in their work on deduced that the electrical conductivity of GrF is majorly influenced by the bending stress at the node and adhesion energy between individual Gr sheets at a characteristic length scale. The length and width of individual Gr sheets forming the holistic GrF also contribute to its electron and phonon transfer phenomenon. Here the LTCC infiltrate exerts compression on the GrF, thus increasing the contact area between individual Gr sheets and thereby increasing the electrical property by contact conductance phenomenon as represented by the schematic in Figure 8. The induced electrical conductivity in the LTCC/GrF is another testament that the reticulated structure of the GrF is intact after SPS. The conductivity can be tailored by GrF content in the ceramic.

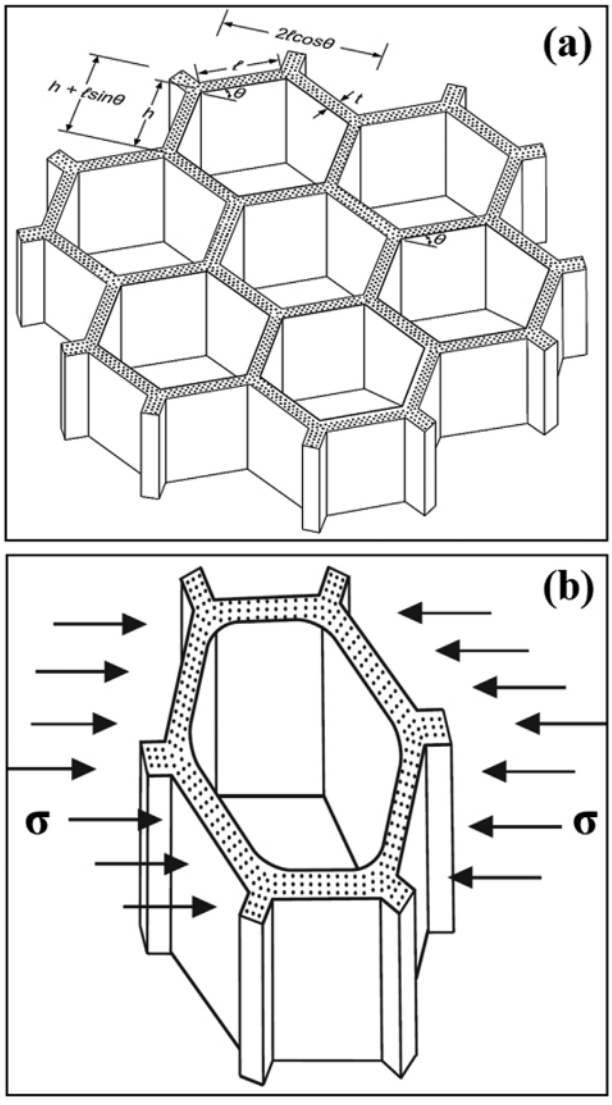

Figure 7. a) Schematic representing the cell geometry of GrF cell; b) schematic representing cell wall deflection upon stress (σ).

Figure 8. Schematic depicting the charge transfer (charge represented in blue) scheme in the case of GrF made with multiple Gr sheets.

To assess the influence of the GrF foam on the thermal property of the material, thermal analysis using the infrared camera was conducted. LTCC/GrF material and pure LTCC samples were placed on an isothermal hotplate maintained at 100 °C. The change in sample temperature with time was monitored for both the samples as shown in Video S2, Supporting information. **Figure 9** shows thermal images of the samples at different time stamp and samples temperature.

From Figure 9, two obvious observations can be made:

i The LTCC/GrF material conducts heat at a higher rate than pure LTCC sample
ii The LTCC/GrF material conducts heat uniformly across the bulk as observed by uniform coloration of the test sample

At a very low wt% (0.18) of GrF, the material not only exhibited improved mechanical properties but also display enhanced electrical and thermal conductivity due to phonon transfer. Though the improvement in thermal conductivity is in the range of 1 °C s^{-1}, it must be noted that the only 20 mm^3 of GrF is present within ≈638 mm^3 of the cylindrical bulk composite (Figure S3, Supporting Information).

By controlling the wt% of GrF, one can fine tune the thermal and electrical properties of the material along with proactive mechanical enhancement. The highly reticulated 3D architecture of the GrF opens the gateway for advanced engineering materials development and can form improved ceramic packaging materials. Though in the past only low viscous polymer/GrF materials were fabricated, a simple methodology to fabricate closed cell, fully embedded GrF ceramic is elaborated. The ceramic infiltration technique developed in this work can be used in the production of medical implants or sensors. The methodology developed will enable the development of various GrF based ceramic composites with improved mechanical, electrical, and thermal properties.

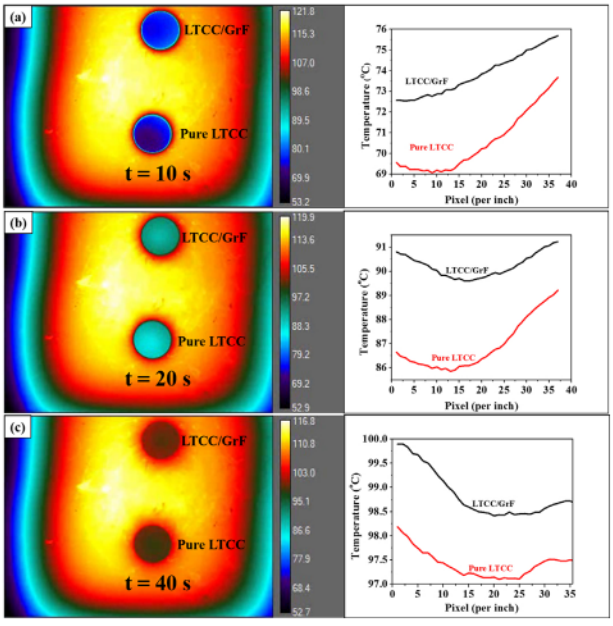

Figure 9. Thermal images of LTCC/GrF and pure LTCC sample. a) At time 10 s; b) 20 s; and c) 40 s. The X-axis represent Pixel per inch of the cylindrical sample only.

3. Conclusion

A 3D Graphene Foam-based ceramic composite is fabricated in this study to achieve superior structural and thermo-electrical transport characteristics in LTCC. A novel three-step processing scheme was adopted to engineer a unique composite microstructure, consisting of a 3D network of graphene in an α-Al_2O_3 -Ca(Si, Al)$_4O_8$ based LTCC system. The interconnected node-branch architecture of embedded graphene foam provides pathways for stress, electron and phonon transfer in the composite. This resulted in a multifunctional composite with enhanced properties by adding merely 0.18 wt% GrF:

1) Fracture energy was found to increase by 480% by adding GrF. Sub-surface microscopy revealed extensive crack deflection by a 3D cellular network of GrF as the responsible mechanism.
2) High load indentation showed a 23% improvement in elastic modulus, indicating graphene filler induced stiffening and effective load transfer from LTCC to GrF.
3) The addition of GrF induced an impressive electrical conductivity of 165 S m^{-1} in an otherwise insulating LTCC.
4) In situ infrared thermal imaging at elevated temperatures showed a higher rate of temperature rise for GrF reinforced sample when subjected to heating.

This study highlights the promise of 3D GrF as a filler material for developing high performance, multifunctional ceramic composites. The proposed three-step processing technique can be extended to other ceramic systems to incorporate pre-fabricated graphene frameworks for superior properties. This new class of composites can provide structural support/ load bearing ability, thermal management as well as electrical transport. The potential applications include spacecraft bodies, MEMS/NEMS, robotics, advanced sensors, electronic devices, and resilient bio-implants.

4. Experimental Section

Commercially available free-standing GrF from Graphene Supermarket (Calverton, NY, USA) was used in this study. The low-temperature co-fired ceramic (LTCC) powder was obtained from Dupont (Wilmington, DE, USA) commercially known as Dupont 951. Though the exact composition of the powder is proprietary, the major phase structure is composed of α-Al_2O_3 and Ca (Si, Al)$_4O_8$. A three-steps Infiltration-Solidification-Spark plasma Sintering (SPS) method is adapted in the present work to produce LTCC/GrF composite material. The viscosity of the ceramic slurry was measured by Brooksfield DV-II viscometer. SPS was performed at 700 °C for 15 min at 50 °C min^{-1} applying a pressure of 100 MPa.

Field-emission scanning electron microscope (FE-SEM JEOL JSM-6330F, JEOL Ltd. Tokyo, Japan) was employed to inspect the top and fracture surfaces of both pure LTCC and LTCC/GrF samples. Optical Microscope (Versamet 3, Buehler, Lake Bluff, IL, USA) was used to ensure the retention of GrF's 3D architecture after each processing step. Mechanical properties were analyzed on sintered pellets. A *high load* (100 N) instrumented indentation was also performed by a linear, screw

driven micro-load frame (SEM Tester 1000, MTI Instruments Inc. USA.) with a Vickers tip attached. Indentation tests were carried out on a polished surface with a maximum displacement of 0.25 mm. Multi-Beam Focused Ion Beam (FIB, JEOL-JIB 4500, JEOL Ltd. Tokyo, Japan) was employed in milling the cracked surface to understand the sub-surface fracture mechanism in the LTCC/GrF composite material. The electrical conductivity of the novel LTCC/GrF material was evaluated from DC four-point-probe method using Keithly 2401 digital multimeter at room temperature and pressure. A T450 sc thermal imaging camera from FLIR was employed for thermal studies.

Supporting Information

Supporting Information is available from the Wiley Online Library or from the author.

Acknowledgments

TT, PN, and AA acknowledge the Engineering Research Centers Program of the National Science Foundation under NSF Cooperative Agreement No. EEC-1647837. PN thanks Florida International University (FIU) Graduate School for the Presidential Fellowship award. Advanced Materials Engineering Research Institute (AMERI) at FIU is acknowledged for the research facilities used in this study.

Conflict of Interest

The authors declare no conflict of interest.

Keywords

3D graphene foam, electrical, LTCC, mechanical properties, novel composite, SPS, thermal

Received: January 21, 2019
Revised: February 26, 2019
Published online:

[1] A. K. Geim, *Science* **2009**, *324*, 1530.
[2] S. Stankovich, D. A. Dikin, G. H. B. Dommett, K. M. Kohlhaas, E. J. Zimney, E. A. Stach, R. D. Piner, S. T. Nguyen, R. S. Ruoff, *Nature* **2006**, *442*, 282.
[3] T. Ramanathan, A. A. Abdala, S. Stankovich, D. A. Dikin, M. H. Alonso, R. D. Piner, D. H. Adamson, H. C. Schniepp, X. Chen, R. S. Ruoff, S. T. Nguyen, I. A. Aksay, R. K. Prud'Homme, L. C. Brinson, *Nature Nanotechnol.* **2008**, *3*, 327.
[4] X. Li, X. Wang, L. Zhang, S. Lee, H. Dai, *Science* **2008**, *319*, 1229.
[5] F. Schwierz, *Nature Nanotechnol.* **2010**, *5*, 487.
[6] X. Huang, Z. Zeng, Z. Fan, J. Liu, H. Zhang, *Adv. Mater.* **2012**, *24*, 5979.
[7] L. Fontoura, P. Nautiyal, A. Loganathan, B. Boesl, A. Agarwal, *Adv. Eng. Mater.* **2018**, *20*, 1800518.
[8] J. Bustillos, D. Montero, P. Nautiyal, A. Loganathan, B. Boesl, A. Agarwal, *Polym. Compos.* **2017**, *39*, 3877.
[9] C. Lee, X. Wei, J. W. Kysar, J. Hone, *Science* **2008**, *321*, 385.
[10] A. A. Balandin, S. Ghosh, W. Bao, I. Calizo, D. Teweldebrhan, F. Miao, C. N. Lau, *Nano Lett.* **2008**, *8*, 902.
[11] A. K. Geim, K. S. Novoselov, *Nature Mater.* **2007**, *6*, 183.
[12] A. Nieto, A. Bisht, D. Lahiri, C. Zhang, A. Agarwal, *Int. Mater. Rev.* **2017**, *62*, 241.
[13] D. Li, M. B. Muller, S. Gilje, R. B. Kaner, G. G. Wallace, *Nature Nanotechnol.* **2008**, *3*, 101.
[14] D. Lahiri, R. Dua, C. Zhang, I. Soccarraz-Novoa, A. Bhat, S. Ramaswamy, A. Agarwal, *ACS Appl. Mater. Interf.* **2012**, *4*, 2234.
[15] L. C. Tang, Y. J. Wan, D. Yan, Y. B. Pei, L. Zhao, Y. B. Li, L. B. Wu, J. X. Jiang, G. Q. Lai, *Carbon* **2013**, *60*, 16.
[16] Q. Wu, Y. Xu, Z. Yao, A. Liu, G. Shi, *ACS Nano* **2010**, *4*, 1963.
[17] V. H. Pham, T. T. Dang, S. H. Hur, E. J. Kim, J. S. Chung, *ACS Appl. Mater. Interf.* **2012**, *4*, 2630.
[18] D. Esrafilzadeh, R. Jalili, E. M. Stewart, S. H. Aboutalebi, J. M. Razal, S. E. Moulton, G. G. Wallace, *Adv. Funct. Mater.* **2016**, *26*, 3105.
[19] K. Wang, H. Wu, Y. Meng, Z. Wei, *Small* **2014**, *10*, 14.
[20] Z. Song, T. Xu, M. L. Gordin, Y. B. Jiang, I. T. Bae, Q. Xiao, H. Zhan, J. Liu, D. Wang, *Nano Lett.* **2012**, *12*, 2205.
[21] Y. Fu, L. Liu, J. Zhang, *ACS Appl. Mater. Interf.* **2014**, *6*, 14069.
[22] P. Nautiyal, L. Embrey, B. Boesl, A. Agarwal, *Carbon* **2017**, *122*, 298.
[23] L. Qiu, J. Z. Liu, S. L. Y. Chang, Y. Wu, D. Li, *Nat. Commun.* **2012**, *3*, 1241.
[24] M. Wang, X. Duan, Y. Xu, X. Duan, *ACS Nano* **2016**, *10*, 7231.
[25] Y. Meng, K. Wang, Y. Zhang, Z. Wei, *Adv. Mater.* **2013**, *25*, 6985.
[26] Z. Qin, G. S. Jung, M. J. Kang, M. J. Buehler, *Sci. Adv.* **2017**, *3*, e1601536.
[27] K. Shehzad, Y. Xu, C. Gao, X. Duan, *Chem. Soc. Rev.* **2016**, *45*, 5541.
[28] C. Zhu, T. Y. J. Han, E. B. Duoss, A. M. Golobic, J. D. Kuntz, C. M. Spadaccini, M. A. Worsley, *Nat. Commun.* **2015**, *6*, 6962.
[29] Y. Wu, N. Yi, L. Huang, T. Zhang, S. Fang, H. Chang, N. Li, J. Oh, J. A. Lee, M. Kozlov, A. C. Chipara, H. Terrones, P. Xiao, G. Long, Y. Huang, F. Zhang, L. Zhang, X. Lepro, C. Haines, M. D. Lima, N. P. Lopez, L. P. Rajukumar, A. L. Elias, S. Feng, S. J. Kim, N. T. Narayanan, P. M. Ajayan, M. Terrones, A. Aliev, P. Chu, Z. Zhang, R. H. Baughman, Y. Chen, *Nat. Commun.* **2015**, *6*, 6141.
[30] Z. Chen, W. Ren, L. Gao, B. Liu, H. M. Cheng, *Nature Mater.* **2011**, *10*, 424.
[31] C. Wang, C. Zhang, S. Chen, *Carbon.* **2016**, *109*, 666.
[32] Y. R. Jeong, H. Park, S. W. Jin, S. Y. Hong, S. S. Lee, J. S. Ha, *Adv. Funct. Mater.* **2015**, *25*, 4228.
[33] Z. Chen, C. Xu, C. Ma, W. Ren, H. M. Cheng, *Adv. Mater.* **2013**, *25*, 1296.
[34] A. Nieto, R. Dua, C. Zhang, B. Boesl, S. Ramaswamy, A. Agarwal, *Adv. Funct. Mater.* **2015**, *25*, 3916.
[35] J. Jia, X. Sun, X. Lin, X. Shen, Y. W. Mai, J. K. Kim, *ACS Nano* **2014**, *8*, 5774.
[36] J. Bustillos, C. Zhang, B. Boesl, A. Agarwal, *ACS Appl. Mater. Interf.* **2018**, *10*, 5022.
[37] A. Idowu, B. Boesl, A. Agarwal, *Carbon* **2018**, *135*, 52.
[38] P. Nautiyal, M. Mujawar, B. Boesl, A. Agarwal, *Carbon* **2018**, *137*, 502.
[39] A. Nieto, B. Boesl, A. Agarwal, *Carbon* **2015**, *85*, 299.
[40] P. Nautiyal, B. Boesl, A. Agarwal, *Carbon* **2018**, *132*, 59.
[41] P. Nautiyal, B. Boesl, A. Agarwal, *Small* **2017**, *13*, 1603473.
[42] L. Embrey, P. Nautiyal, A. Loganathan, A. Idowu, B. Boesl, A. Agarwal, *ACS Appl. Mater. Interf.* **2017**, *9*, 39717.
[43] H. Fang, Y. Zhao, Y. Zhang, Y. Ren, S. L. Bai, *ACS Appl. Mater. Interf.* **2017**, *9*, 26447.
[44] J. Liu, X. Wang, T. Wang, D. Li, F. Xi, J. Wang, E. Wang, *ACS Appl. Mater. Interf.* **2014**, *6*, 19997.
[45] Y. C. Yong, X. C. Dong, M. B. Chan-Park, H. Song, P. Chen, *ACS Nano* **2012**, *6*, 239.
[46] Y. Qiu, J. Liu, Y. Lu, R. Zhang, W. Cao, P. Hu, *ACS Appl. Mater. Interf.* **2016**, *8*, 18496.
[47] W. Wei, S. Yang, H. Zhou, I. Lieberwirth, X. Feng, K. Müller, *Adv. Mater.* **2013**, *25*, 2909.

[48] Y. He, W. Chen, X. Li, Z. Zhang, J. Fu, C. Zhao, E. Xie, *ACS Nano* **2013**, *7*, 174.
[49] H. Y. Yue, S. Huang, J. Chang, C. Heo, F. Yao, S. Adhikari, F. Gunes, L. C. Liu, T. H. Lee, B. Li, J. J. Zhang, T. Q. Huy, N. V. Luan, Y. H. Lee, *ACS Nano* **2014**, *8*, 1639.
[50] J. Ru, Y. Fan, W. Zhou, Z. Zhou, T. Wang, R. Liu, J. Yang, X. Lu, J. Wang, C. Ji, L. Wang, W. Jiang, *ACS Appl. Mater. Interfaces* **2018**, *10*, 39245.
[51] L. E. Khoong, Y. M. Tan, Y. C. Lam, *J. Eur. Ceram. Soc.* **2010**, *30*, 457.
[52] S. K. Reddy, D. B. Ferry, A. Misra, *RSC. Adv.* **2014**, *4*, 50074.
[53] W. Xie, F. Song, R. Wang, S. Sun, M. Li, Z. Fan, B. Liu, Q.G. Zhang, J. Wang, *Crystals* **2018**, *8*, 1.
[54] K. Bumsu, Y. H. Lee, J. H. Ryu, K. D. Suh, *Colloids Surf. Physicochem. Eng. Aspects* **2006**, *273*, 161.
[55] Y. Gao, T. Cao, F. Cellini, C. Berger, W. A. de Heer, E. Tosatti, E. Riedo, A. Bongiorno, *Nat. Nanotech.* **2018**, *13*, 133.
[56] L. J. Gibson, M. F. Ashy, B. A. Harley, Cellular materials in nature and medicine, *Cambridge* **2010**, ISBN 978-0-521-19544-7.
[57] G. I. Barenblatt, *Adv. Appl. Mech.* **1962**, *7*, 55.
[58] F. Liu, C. Wang, Q. Tang, *Small* **2018**, *14*, 1801458.

